Materials Advances

Accepted Manuscript

This article can be cited before page numbers have been issued, to do this please use: M. Sivakumar, J. Prasath, S. Senthamizh Raja, A. V. Rose, J. Mani, L. C. Chuang, S. S. S. Gadhavajhala, B. Srinivasan, J. Ramasamy, K. Fujiwara and M. Arivanandhan, *Mater. Adv.*, 2026, DOI: 10.1039/D6MA00062B.

ROYAL SOCIETY OF CHEMISTRY

rsc.li/materials-advances

View Article Online
DOI: 10.1039/D6MA00062B

Grain Structure–Controlled Growth of InSb Crystals: A Grain Boundary Engineering Approach for Enhanced Thermoelectric Performance

M. Sivakumar[a], J. Prasath[a] , S. Senthamizh Raja[a] , R. Annie Victoria Rose[a], J. Mani[b], L.C. Chuang[c] , Sri Sai Samhitha Gadhavajhala[d], Bhuvanesh Srinivasan[d], R. Jayavel[e], K. Fujiwara[c], M. Arivanandhan[a*]

[a] Centre for Nanoscience and Technology, Anna University, Chennai-600 025, Tamil Nadu, India.

[b]MoE Key Laboratory of Material Physics and Chemistry Under Extraordinary Conditions, School of Physical Science and Technology, Northwestern Polytechnical University, Xi'an – 710072, People's Republic of China.

[c]Institute for Materials Research, Tohoku University, Sendai - 980 8577, Japan.

[d] Department of Metallurgical and Materials Engineering, Indian Institute of Technology Madras (IIT-Madras), Chennai 600 036, Tamil Nadu, India.

[c] Crystal Growth Centre, Anna University, Chennai-600 025, Tamil Nadu, India.

Abstract

The InSb polycrystalline ingots were prepared by direct melt quenching method under different cooling rates of slow cooling (SC), air quenching (AQ), and ice water quenching (IWQ). The crystal structure and grain structure of InSb ingots have been analysed by XRD and FESEM. The variation in grain structure, grain orientation, and grain boundaries of the samples with different cooling rates were analysed by EBSD. The Seebeck coefficient (S) of InSb samples decreased with respect to cooling rates owing slight decrease in the electrical resistivity. A high-power factor (PF) of 6951 µW/m K^2 was achieved for IWQ sample at 573 K compared to SC InSb sample (5935 µW/m K2 at 573 K). The thermal conductivity is relatively decreased for IWQ InSb sample (6.60 W/m/K @ 573 K) compared to SC InSb (7.29 W/m.K @ 573 K) due to modification in the grain structures, grain boundary densities and grain boundary characters of InSb during rapid cooling, which enhanced the phonon scattering in IWQ sample. Subsequently, high zT of 0.60 was achieved at 573 K for IWQ InSb sample compared to the SC InSb (zT of 0.46 at 573 K).

Key Words: InSb, Melt Quenching, Controlled grain growth, Phonon scattering, Thermoelectrics.

*Corresponding author: M. Arivanandhan

E-mail: arivucz@gmail.com

1. Introduction

Electrical energy is very significant for all sectors in this modernized world. The demand for electric energy is hastily rising due to the increasing global human population[1]. Furthermore, the high amount of burning of fossil fuels emits CO_2 emission which leads to an increase the Global warming[2,3]. Hence, an alternative and sustainable energy is needed to fulfil the energy requirement as well as the energy demand. Such a kind of clean energy is more important for a green and pollution-free environment to realize the sustainable developments[4–6]. In industries and automobiles lot of energy is unused in the form of heat energy[7,8]. Thermoelectric (TE) technology is a promising technology to convert this kind of waste heat into useful electricity through the principle of the Seebeck effect[9,10]. A thermoelectric device consists of p-type and n-type materials which connected electrically in series and thermally in parallel. The TE technology is pollution-free, environmentally friendly, with non-movable parts offering practical operational integration[11]. The TE technology is very useful in various aspects such as thermoelectric generators, wearable watches, Peltier modules, sensors, and electronic gadgets. The performance of a TE functional material is based on the figure of merit (zT) which is shown in the following eqn. (1),

$$zT = \frac{S^2}{\rho \kappa_T} T \quad (1)$$

where S is the Seebeck coefficient, ρ is the electrical resistivity, and κ_T is total thermal conductivity, T-Absolute Temperature[12] . A good thermoelectric material should have zT >1, then only it's possible to use it in practical applications. The high zT can be attained by increasing the power factor (PF) (PF = $\frac{S^2}{\rho}$) and dropping the thermal conductivity[13]. The PF can be enhanced by hetero valence substitution[14,15], doping[12,16,17] and compositing[18–20] , nano-inclusions[21–23]. The thermal conductivity can be suppressed through nano-structuring[24–26] the material, defect engineering[27–29], point defect scattering[27,28], grain boundary engineering[30,31] and phonon engineering[24,32–35], Melt Quenching[32,36]. Good thermoelectric

View Article Online
DOI: 10.1039/D6MA00062B

materials behave like phonon glass – electron crystal (PGEC)[33]. But, in general, the thermal and electrical conductivities are coupled together. So, it's quite difficult to enhance the performance of TE energy harvesting materials by decoupling the electrical and thermal conductivities. Semiconductors are suitable materials for improving the zT value of the material[37]. Because semiconductors have optimum carrier concentration and tunable bandgap as well as low thermal conductivity[38]. A lot of semiconductor materials exhibited high TE performance. Bi_2Te_3[36,37] and $Si_{1-x}Ge_x$ [39]are the familiar semiconductor materials for low and high-temperature TE applications, respectively. However, an appropriate functional material for mid-temperature TE applications is still lagging, despite high performance in a few materials like SnSe and GeTe[40,41].

InSb is a narrow bandgap semiconductor with a bandgap of 0.18 eV and suitable for TE applications[42]. The material has high mobility (μ) and carrier concentration (n) in the range of 10^4 - 10^5 $cm^2V^{-1}S^{-1}$, ~10^{17} cm^{-3} respectively[43,44]. Besson et.al prepared sphalerite-structured InSb nanoparticles by alloying Sb with Indium nano clusters[45]. Cheng et.al. reported a melt-quenched polycrystalline $InSb_{1.04}$ ingots with a zT value 1.28 @773 K[46]. Min Jin et.al. prepared InSb ingots by the Bridgman technique and achieved zT of 0.63 at 700 K[44]. Kang Wang et.al. reported zT of 0.4 for the melt-quenched InSb sample[47]. Yamaguchi et.al. achieved zT of 0.60 at 673 K, which was grown by the Czochralski method[48]. Kaiqi Zhang et.al reported $AgSb_{0.973}$ $Cd_{0.017}$ Se_2 crystal with high thermoelectric ZT of 1.7 at 723 K through Bridgman crystal growth technique[31]. Qi-Qi Wang et.al reported high ZT of ~0.9 at 300 K as well as excellent average ZT of 1.26 through In-situ Loading Bridgman Growth method[30]. But the high thermal conductivity (~16 - 18 $Wm^{-1}K^{-1}$ 300 K) affects the zT of InSb material, which limits its practical applications[46]. Therefore, it is highly essential to reduce the thermal conductivity of InSb for enhancing the zT[49,50]. Developing new strategies like nanostructuring[51], grain boundary engineering[30,31], and nano inclusions[52] is imperative for suppressing the thermal conductivity of InSb. Among these strategies, rapid melt quenching is one of the bulk preparation processes to prepare the InSb with controlled grain structures. This technique effectively controls the grain structure and thereby the grain boundaries. The grain boundaries are the active regions for controlling the thermal conductivity through effective phonon scattering. The manipulation of the grain boundary through the crystallization process is an effective strategy for enhancing the zT. However, this approach has not yet been systematically investigated for InSb. Therefore, in the present work, InSb was crystallized by the melt quenching technique under different cooling rates to manipulate its grain structures. The structural, morphological, and thermoelectric properties of melt-quenched InSb ingots were evaluated. By optimizing the grain structure, the TE performance was greatly enhanced with low thermal conductivity. The thermal conductivity is effectively reduced for IWQ InSb sample (6.60 W/m/K @ 573 K) compared to SC InSb (7.29 W/m. K @ 573 K) due to modification in the grain structures and grain boundary densities which enhanced the phonon scattering in IWQ sample. Subsequently, high zT of 0.60 was achieved at 573 K for IWQ InSb sample compared to the SC InSb (zT of 0.46 at 573 K). The experimental results highlights a simple and scalable microstructure engineering strategy and establishes InSb as a useful material for high-performing thermoelectric systems.

2. Experimental Section:

2.1 Materials

The InSb polycrystals were prepared by the direct melt quenching technique under different cooling rates. The high-purity source materials of Indium shots (6N Purity) and Antimony shots (6N Purity) were purchased from Osaka Chemicals, Japan. The stoichiometric equimolar ratio of (1:1) In and Sb was loaded into a cylinder-shaped quartz ampoule (16 mm inner diameter × 20 mm outer diameter × 15 cm length), and the ampoule was evacuated up to the vacuum pressure of 10^{-5} Torr. The sealed quartz ampoule was sealed and kept in a high-temperature furnace. The temperature of the furnace was increased from room temperature to 640 °C with a ramping rate of 5 °C/min and dwelled at 640 °C for 15 hours to achieve homogeneous melting of indium and antimony shots. After homogeneous melting, the ampoule with the molten sample was cooled at a cooling rate of 1 °C/min to prepare the sample under slow cooling. Similarly, the other two ampoules with In and Sb samples were prepared and melted under identical conditions. After the dwelling period, the ampoules were drastically cooled by air quenching and Ice water quenching processes. After the growth experiment, InSb ingots were cut and polished into rectangular and circular shape samples. These samples were used to measure the TE properties at different temperatures. The prepared slow-cooled, air quenched, and ice water quenched samples were named as SC InSb, AQ InSb and IWQ InSb, respectively. The schematic diagram of the InSb sample preparation procedure is shown in Fig. 1(a). The thermal cycle program used for crystallization under different cooling rates is shown in Fig. 1(b).

View Article Online
DOI: 10.1039/D6MA00062B

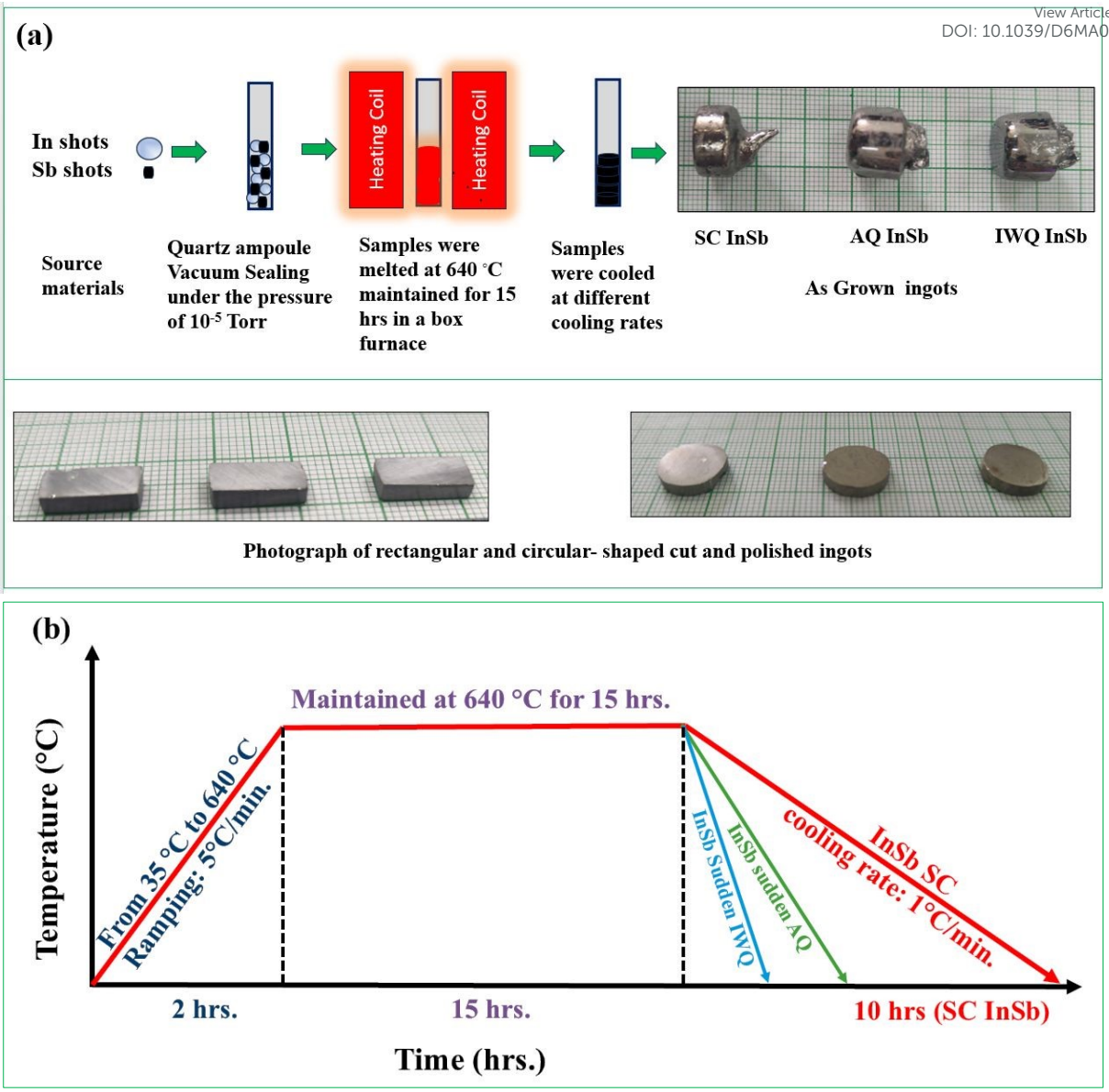

Fig.1: Schematic representation of the sample preparation process (a) and Thermal cycle program (b).

2.2 Characterization

The physicochemical and thermoelectric properties of polycrystalline InSb samples were characterized by various physicochemical characterization techniques such as X-ray Diffraction (XRD), Field Emission Scanning Electron Microscopy (FE-SEM), Energy Dispersive X-ray Spectroscopy (EDX), Electron Back Scatter Diffraction (EBSD), Raman Spectroscopy, X-ray Photoelectron Spectroscopy (XPS), Hall measurements, Seebeck coefficient, and thermal diffusivity measurements. XRD was used to characterize the phase purity and crystal structure of the prepared samples. The analysis was done with a Bruker D8 Advance X-ray diffractometer (Japan), utilizing Cu Kα1 radiation (λ = 1.5406 Å). FE-SEM and EDX analysis revealed the surface grain structure and elemental compositional analysis. These analyses were executed by using a Carl-Zeiss instrument. Raman Spectroscopy analysis was performed to examine the vibrational properties of the InSb samples. A RENISHAW instrument (UK), equipped with a 532 nm laser and a CCD array NIR detector, was used for the analysis. X-ray Photoelectron Spectroscopy (XPS) was used to check the chemical binding states of the samples with the help of a ULVAC instrument. Hall Effect measurements were performed to determine the electrical properties, such as carrier concentration and mobility, of the samples, using an EXCEL India instrument. The Seebeck coefficient and electrical resistivity was measured using ZEM 3 instrument, Advance Riko, Japan. Thermal diffusivity was determined through the laser flash technique using the Netzsch LFA-457 instrument, performed under an argon gas atmosphere. These combined techniques provided a detailed understanding of the structural, morphological, electrical, and thermal characteristics of the prepared InSb samples. The

View Article Online
DOI: 10.1039/D6MA00062B

density of all the samples was calculated for cylindrical shaped ingots. The achieved relative densities of SC, AQ and IWQ InSb are 89.1, 87.2 and 85.3 %, respectively.

3. Results and Discussion

3.1 Structural analysis of InSb samples

Fig. 2 (i)(a) shows the XRD pattern of InSb ingots, it confirms the space group of F-43m with a cubic crystal structure of the InSb ingots. The obtained diffraction peak positions are 23.84˚, 39.45˚, 46.61˚, 56.25˚, 62.76˚, 71.65˚, 76.77˚ for the corresponding planes (111), (220), (311), (400), (331), (422), (511), respectively. All the diffraction peak positions are fine-matched with the JCPDS card no. 06-0208[44,53,54] . Fig. 2(b) shows the enlarged and closer view of the most intense peak hkl value of (111). The intensity of the peak is suppressed for the rapidly cooled samples (AQ and IWQ) compared to the slow-cooled one (SC). Moreover, the peaks are relatively broadened for the AQ and IWQ samples, which is mainly due to higher lattice strain induced by rapid cooling. Ice-water quenching causes rapid cooling that suppresses atomic rearrangement, freezing in fast-growing orientations such as the (311) planes. This results in a preferred (311) texture and an enhanced (311) diffraction peak intensity. The crystallite sizes (D) were calculated by using the following Scherrer's eq. (2).

$$D = \frac{0.9\lambda}{\beta \cos\theta} \quad (2)$$

where D- Crystallite size, λ - X-ray wavelength (1.5406Å), β - full with half maximum (FWHM) and θ - diffraction angle. The lattice strain (β) was calculated by the following eq. (3).

$$\varepsilon = \frac{\beta}{4\tan\theta} \quad (3)$$

The lattice strain and related defects in the crystals facilitate the phonon scattering, which is beneficial for controlling the heat transport. The calculated lattice parameters, lattice micro strain, and crystallite size are listed in Table 1.

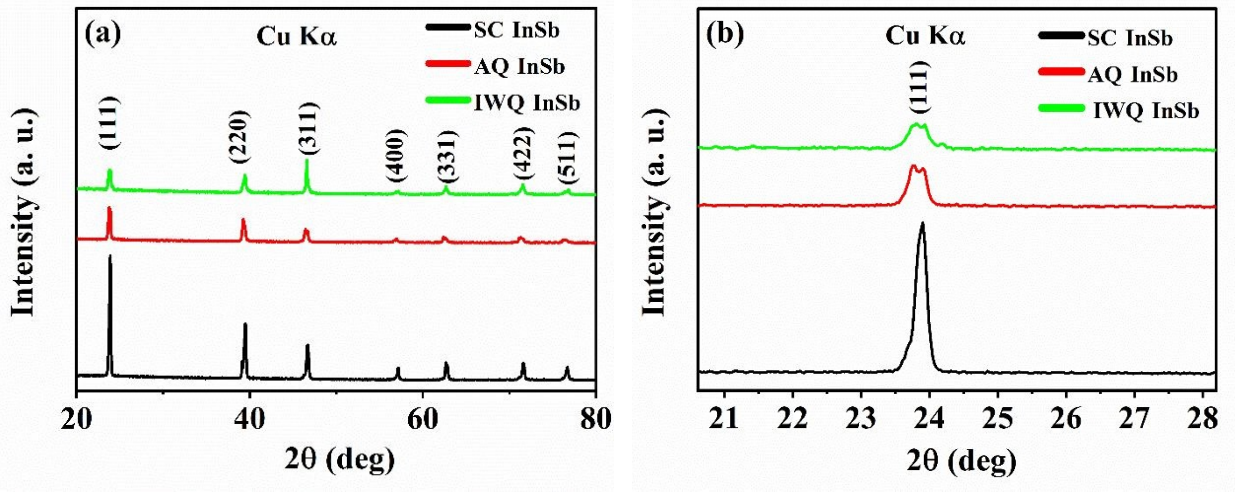

Fig. 2 (i): XRD diffraction patterns of InSb Polycrystalline materials with various cooling rates (a), closer view XRD patterns of (111) plane (b).

Fig. 2 (ii) shows the Rietveld refinement of various cooled samples. The refinement validates the observed changes in lattice parameters and phase purity of SC InSb (a), AQ InSb (b), IWQ InSb (c), samples. Fig.2 (iii) shows the Williamson–Hall Plot (W-H Plot) of SC InSb (a), AQ InSb (b), IWQ InSb (c) Crystal structure (d) of InSb samples. From the W-H plot, the lattice strain and crystallite size were calculated. The crystallite size was decreased with increasing the cooling rate which is mainly due to reduced grain growth. The lattice micro strain was slightly decreased with increasing the cooling rate which is due to Faster cooling can suppress prolonged atomic diffusion. The calculated crystallite size and lattice strain are tabulated in table 1.

View Article Online
DOI: 10.1039/D6MA00062B

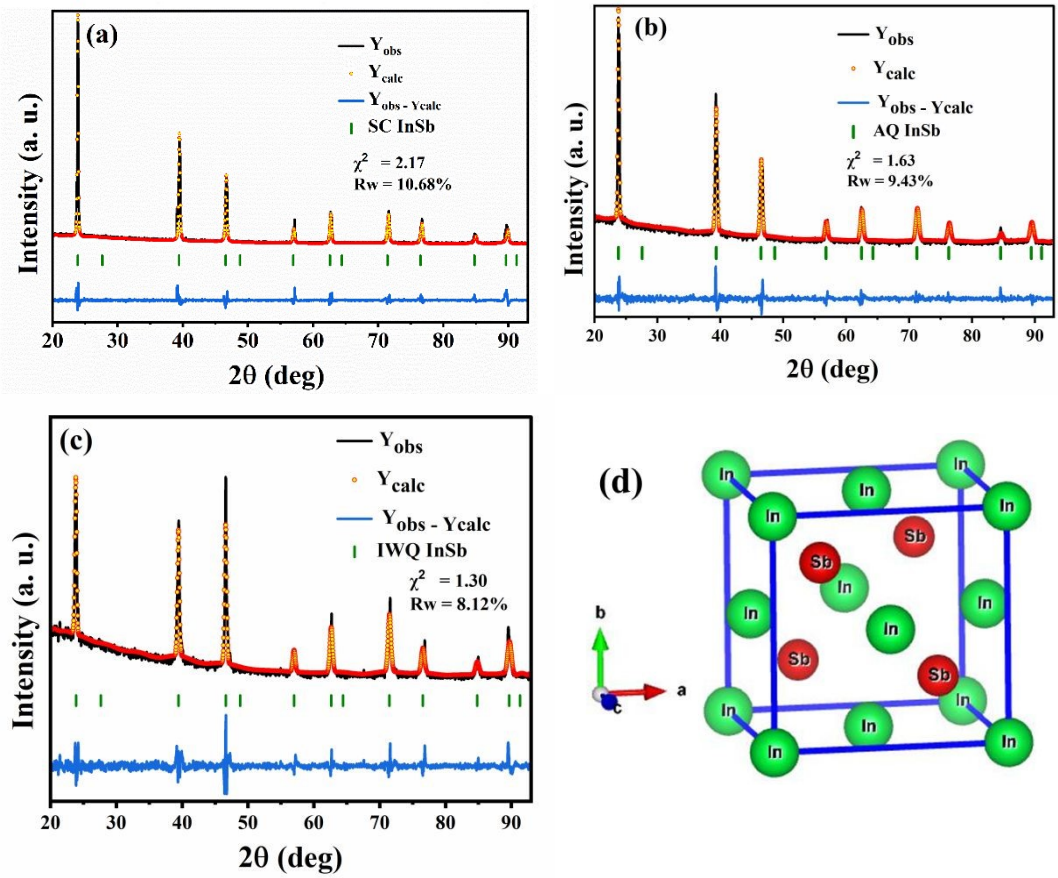

Fig.2 (ii): Rietveld refinement of InSb samples of SC InSb (a), AQ InSb (b), IWQ InSb (c) Crystal structure (d) samples

View Article Online
DOI: 10.1039/D6MA00062B

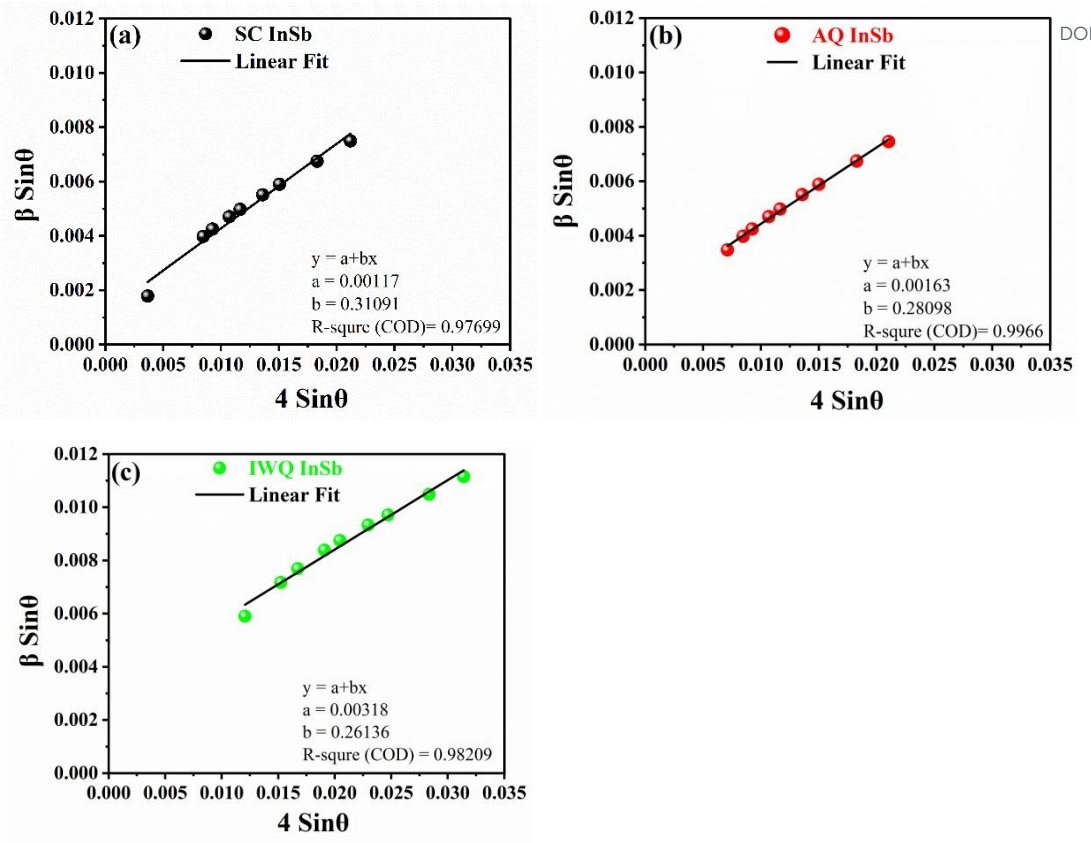

Fig.2 (iii): Williamson–Hall Plot of SC InSb (a), AQ InSb (b), IWQ InSb of InSb samples

Table 1: Lattice parameter, Lattice strain and Crystallite size of InSb samples with different cooling rates.

InSb with cooling rates	Lattice Parameter a (Å)	Crystallite Size (nm)	Lattice Micro strain
SC	6.47	118.5	0.3109
AQ	6.47	85.0	0.2809
IWQ	6.50	43.6	0.2613

3.2 Morphological analysis of the prepared InSb samples

Fig. S1 (a_1-c_3) shows the FESEM images of the prepared ingots SC InSb (a_1-a_3), AQ InSb (b_1-b_3), and IWQ InSb (c_1-c_3) samples. Fig. S2: EDX analysis of SC InSb (a), AQ InSb (b) and IWQ InSb (c), samples. EDX spectrum confirms the presence of In and Sb for each sample The elemental compositions of all the samples are revealed in Table T1. Fig. S3 represents the elemental mapping of SC InSb (a), AQ InSb (b), IWQ InSb (c), samples.

Figure 3 shows the FESEM images and EBSD orientation mappings of SC InSb (a_1-a_2), AQ InSb (b_1-b_2), and IWQ InSb (c_1-c_2) samples with colored standard triangle of orientations. Fig. 3 (a_1), (b_1) and (c_1) were obtained from the centre parts, and Fig. 3 (a_2), (b_2) and (c_2) were from the periphery parts of each sample. The EBSD analysis shows the crystallographic grain structure of the InSb samples with clear grain size variation in all the samples with different cooling rates. The EBSD analysis revealed that the grain growth was decreased with increasing the cooling rates. During the quenching process, the molten InSb solidified rapidly as a function of cooling rates. From the EBSD analysis, the average grain sizes at the centre and edge of the samples were found to be 910 µm and 905 µm in SC InSb, 467 µm and 482 µm in AQ InSb, 213 µm and 158 µm in IWQ InSb, respectively. The coloured standard stereotype triangle shows the different orientations in the grains. During

View Article Online
DOI: 10.1039/D6MA00062B

quenching process, a large number of nucleation were formed in the molten InSb and grown rapidly which restricted the grain growth and end up with fine grain structures. Therefore, the number of grain boundaries increased in IWQ InSb when compared to SC InSb. The grain boundary character distributions of SC InSb, AQ InSb and IWQ InSb samples are shown in the table S4 (a-c). From the table S4 (a) it is obvious that the low angle ∑3 and ∑9 grain boundaries were mainly observed in SC InSb. The Table S4 (b) shows the grain boundary character of AQ InSb sample. In the AQ InSb sample the low angle grain boundaries of ∑3, ∑9 and higher angle grain boundaries of ∑27a, ∑27b, ∑19a were observed. These mixed grain boundaries facilitate to scatter the long-range phonon effectively. The table S4 (c) shows the grain boundary characteristics of IWQ InSb sample. In IWQ InSb sample the low angle grain boundaries of ∑3, ∑9 and higher angle grain boundaries of ∑27a, ∑27b, ∑35b, ∑19b were observed. In this sample more amount of higher angle grain boundaries was present compare to other samples. These more higher angle grain boundaries facilitate effective scattering of the phonons which resulted low κ_T.

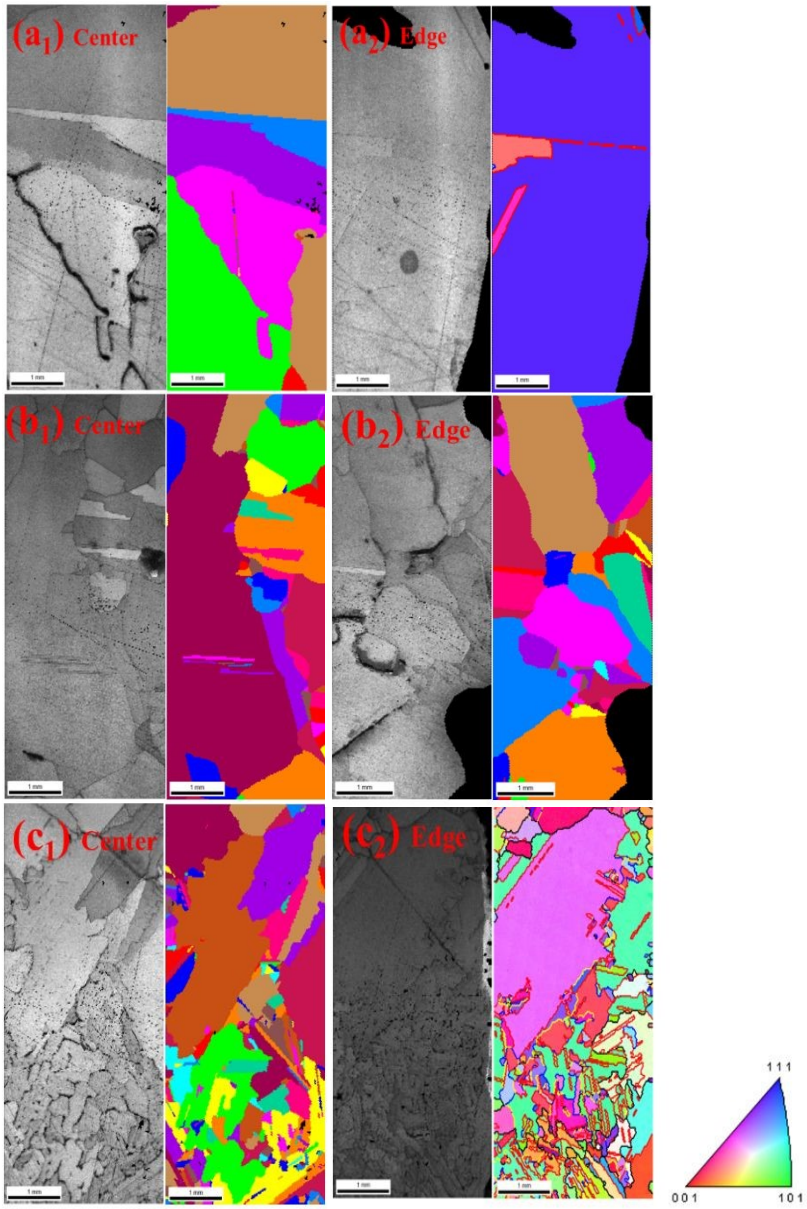

Fig. 3: EBSD images of SC InSb (a_1 – center, a_2- periphery) AQ InSb (b_1- center, b_2- periphery), IWQ InSb (c_1-center, c_2- periphery) samples with colored standard triangle of orientation.

View Article Online
DOI: 10.1039/D6MA00062B

3.3 Raman analysis of InSb samples

Figure 4 shows the Raman spectra of SC InSb (a), AQ InSb (b), and IWQ InSb (c) recorded in the Raman shift range of 111–300 cm^{-1}. The spectra exhibit characteristic vibrational features corresponding to longitudinal optical (LO) and transverse optical (TO) phonon modes of InSb. For SC InSb, Raman peaks are observed at 108 cm^{-1} (A_{1g}), 143 cm^{-1} (A_{1g}), and 177 cm^{-1} (B_{1g}). The AQ InSb sample shows similar modes at 107 cm^{-1} (A_{1g}), 143 cm^{-1} (A_{1g}), and 178 cm^{-1} (B_{1g}). In contrast, IWQ InSb exhibits Raman peaks at 105 cm^{-1} (A_{1g}), 140 cm^{-1} (A_{1g}), 179 cm^{-1} (B_{1g}), and an additional LO mode at 188 cm^{-1} (A_{1g}). All observed Raman modes are in good agreement with previously reported literature values for crystalline InSb[34,53], confirming the successful formation of the InSb phase. The Raman peaks corresponding to the rapidly cooled samples exhibit noticeable broadening and enhanced intensity, which can be attributed to lattice strain and disorder-induced relaxation of Raman selection rules, leading to modified phonon vibrational behaviour. The comparatively higher strain in IWQ InSb, inferred from the pronounced LO mode and peak broadening, is consistent with the XRD results summarized in Table 1, indicating increased lattice distortion caused by rapid quenching.

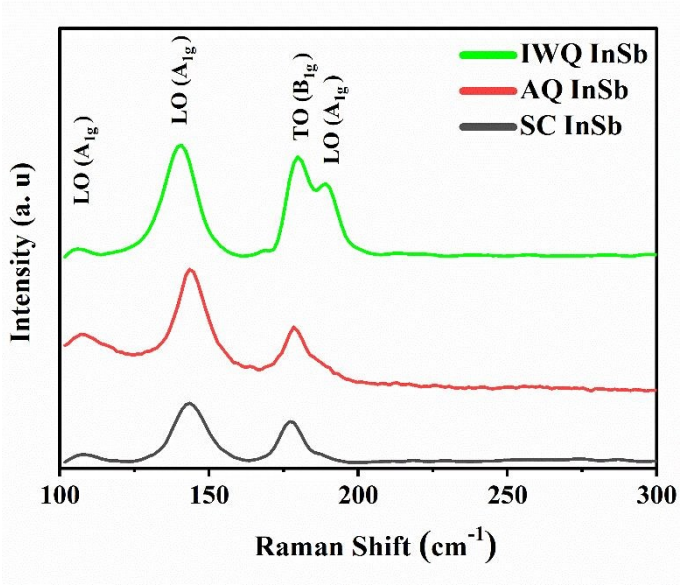

Fig. 4: Raman Spectra of SC InSb (a), AQ InSb (b), IWQ InSb (c), samples.

3.4 Electrical Transport properties of InSb prepared under different cooling rates

The ρ of InSb samples with respect to temperature is shown in Fig. 5 (a). The ρ of all samples decreased with temperature which confirm the semiconductor behaviour of the sample. The ρ was slightly decreased while increasing the cooling rate. The ρ was slightly decreased from 2.74 x 10^{-5} Ω. m (SC InSb sample) to 2.41 x 10^{-5} Ω. m (IWQ InSb sample) at 319 K (Fig. 7 (a)). Fig. 5 (b) shows the variation of n of the prepared InSb samples. The n was almost in the same order of 10^{17} cm^{-3} for all the InSb samples (Fig. 5 (b)). The μ of InSb was slightly increased from 1280 $Cm^2v^{-1}s^{-1}$ (InSb SC sample) to 1508 $Cm^2v^{-1}s^{-1}$ (IWQ sample) while increasing the cooling rates (Fig. 5 (c)). The slight decrease in ρ with increasing cooling rate is possibly due to the presence of higher angle grain boundaries in the rapidly cooled samples as observed in the EBSD analysis. The higher angle grain boundaries result higher μ in the samples which resulted low resistivity in the rapidly cooled samples despite of same range of n values.

View Article Online
DOI: 10.1039/D6MA00062B

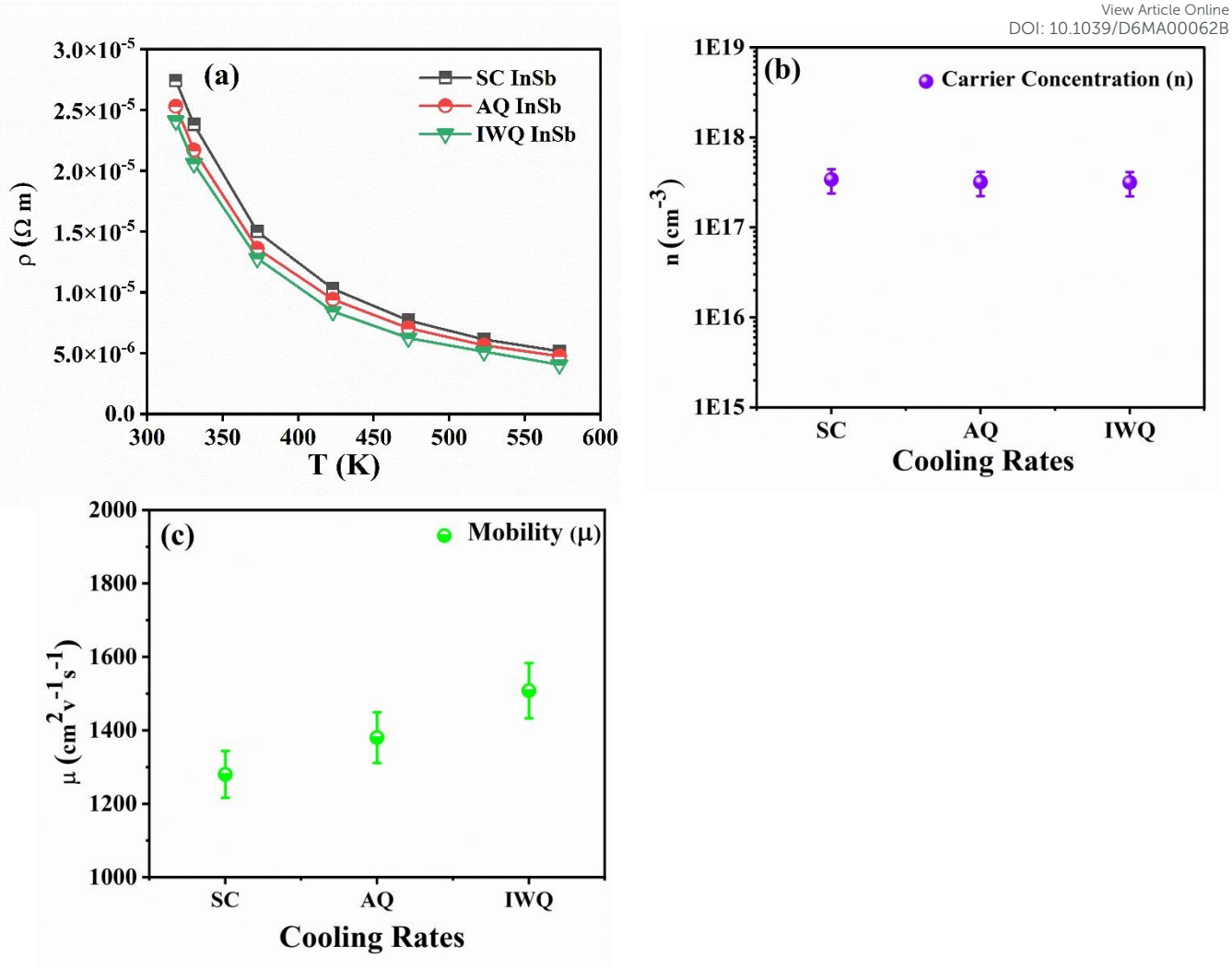

Fig. 5: Variation of ρ as a function of temperature (a), variation of n (b) and variation of μ of SC InSb, AQ InSb, IWQ InSb samples.

View Article Online
DOI: 10.1039/D6MA00062B

3.5 Seebeck Co-efficient of InSb samples:

Figure 6 (a) shows the Seebeck coefficients (S) of all InSb ingots as a function of temperature. The S values of all the InSb samples show negative values, which indicates that all the prepared samples have n-type semiconducting behaviour. The S value decreased with increasing cooling rate due to low ρ values of the samples. The SC InSb shows high S of -245 µV/K at 319 K compared to IWQ InSb (-233 µV/K at 319 K). The decrease in S with increasing temperature is attributed to intrinsic carrier excitation and the resulting bipolar conduction in narrow bandgap InSb, where thermally generated minority carriers reduce the net S through carrier compensation.

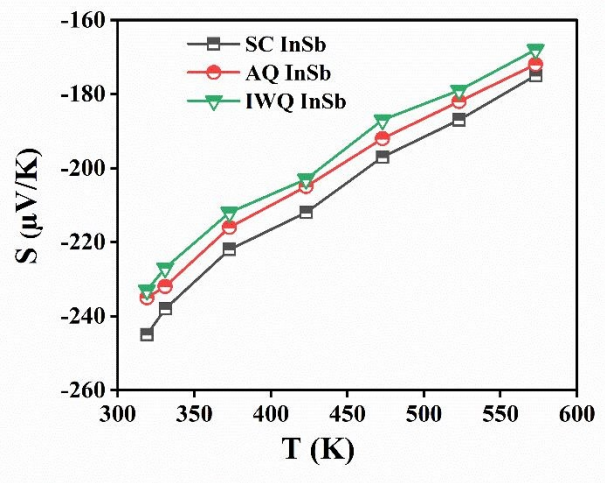

Fig. 6: Seebeck coefficient of SC InSb, AQ InSb and IWQ InSb samples.

3.6 Thermoelectric Power factor of InSb samples:

The PF of the samples was calculated from the measured S and ρ values at different temperatures. Figure 7 shows the variations of PF of InSb samples prepared at different cooling rates. A high PF of 6951 µW/m K^2 was achieved for IWQ InSb at 573 K compared to SC InSb sample (5935 µW/m K^2) at 573 K. The low ρ values of fine grain structured IWQ InSb sample resulted in high PF compared to other samples.

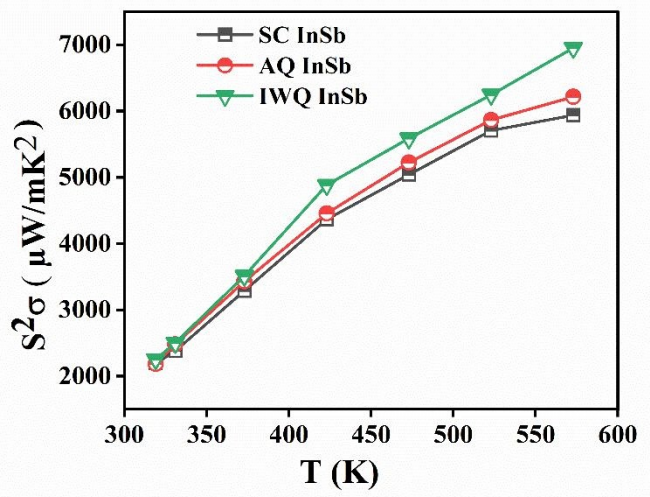

Fig. 7: Temperature dependent Power factor of SC InSb, AQ InSb, IWQ InSb samples

View Article Online
DOI: 10.1039/D6MA00062B

3.7 Thermal conductivity measurement of InSb:

Fig. 8 (a) displays the κ_T of various cooled InSb with respect to temperature. The κ_T is the combination of electronic thermal conductivity (κ_e) and lattice thermal conductivity (κ_T), which is represented by the following eq. (4)[55,56].

$$\kappa_T = \kappa_e + \kappa_L \quad (4)$$

The κ_T was decreased with increasing the cooling rate of the samples. The SC InSb has the κ_T of 7.29 W/m. K at 573 K and it reduced to 6.60 W/m.K at the same temperature for the IWQ InSb. Fig. 8 (b) shows the κ_e of the InSb samples with various temperature. The κ_e was calculated by using the following eq. (5).

$$\kappa_e = \frac{LT}{\rho} \quad (5)$$

Fig. 8 (c) shows the temperature dependant Lorentz number (L) of the prepared InSb samples with different cooling rates. The magnitude of L was calculated by using the measured S values and their relations as shown in the following (eqn. (7)) [55,56.]

$$L = 1.5 + \exp\{-\frac{|s|}{116}\} \quad (7)$$

The L was increased as a function of cooling rate due to the decrease in the ρ.

The κ_e was increased due to decrease in the ρ of the samples with the cooling rate. Fig. 8 (d) illustrates the κ_L of the InSb samples as a function of temperatures. The κ_L was extracted by subtracting the κ_e from κ_T, using the following eq. (6) [57].

$$\kappa_L = \kappa_T - \kappa_e = \kappa_T - \frac{LT}{\rho} \quad (6)$$

The κ_L was decreased with increasing the cooling rates of the sample. The κ_L decreased with increasing temperature due to enhanced phonon–phonon Umklapp scattering, which reduces the phonon mean free path at elevated temperatures. In addition, the EBSD images confirm the systematic reduction in grain size at centres and edges from 910 µm and 905 µm in SC InSb sample to 213 µm and 158 µm in IWQ sample, respectively, leading to a significant increase in grain boundary density. These grain boundaries act as effective phonon scattering centers, which further limits thermal transport. The combined effect of intrinsic phonon–phonon scattering and extrinsic grain boundary scattering results in a pronounced suppression of κ_L, particularly in the fine-grain structured IWQ InSb samples. The grain boundary character distributions of SC, AQ, and IWQ InSb samples are shown in Table S4 (a–c). SC InSb contains only low-angle Σ3 and Σ9 boundaries, resulting in weaker phonon scattering and resulted higher lattice thermal conductivity (κ). In the AQ InSb sample, additional high-angle boundaries (Σ27a, Σ27b, Σ19a) were present, which enhances phonon scattering and reduced κ_L. IWQ InSb contains the highest fraction of higher angle boundaries (Σ27a, Σ27b, Σ35b, Σ19b), leading to the strongest phonon scattering which resulted the lowest κ_L among all samples. Fig. 8 (e) shows the thermal conductivity comparisons with reported values of similar materials[46,48,49,53,58,59]. The measured thermal conductivity of the samples are relatively lower than that of reported values.

View Article Online
DOI: 10.1039/D6MA00062B

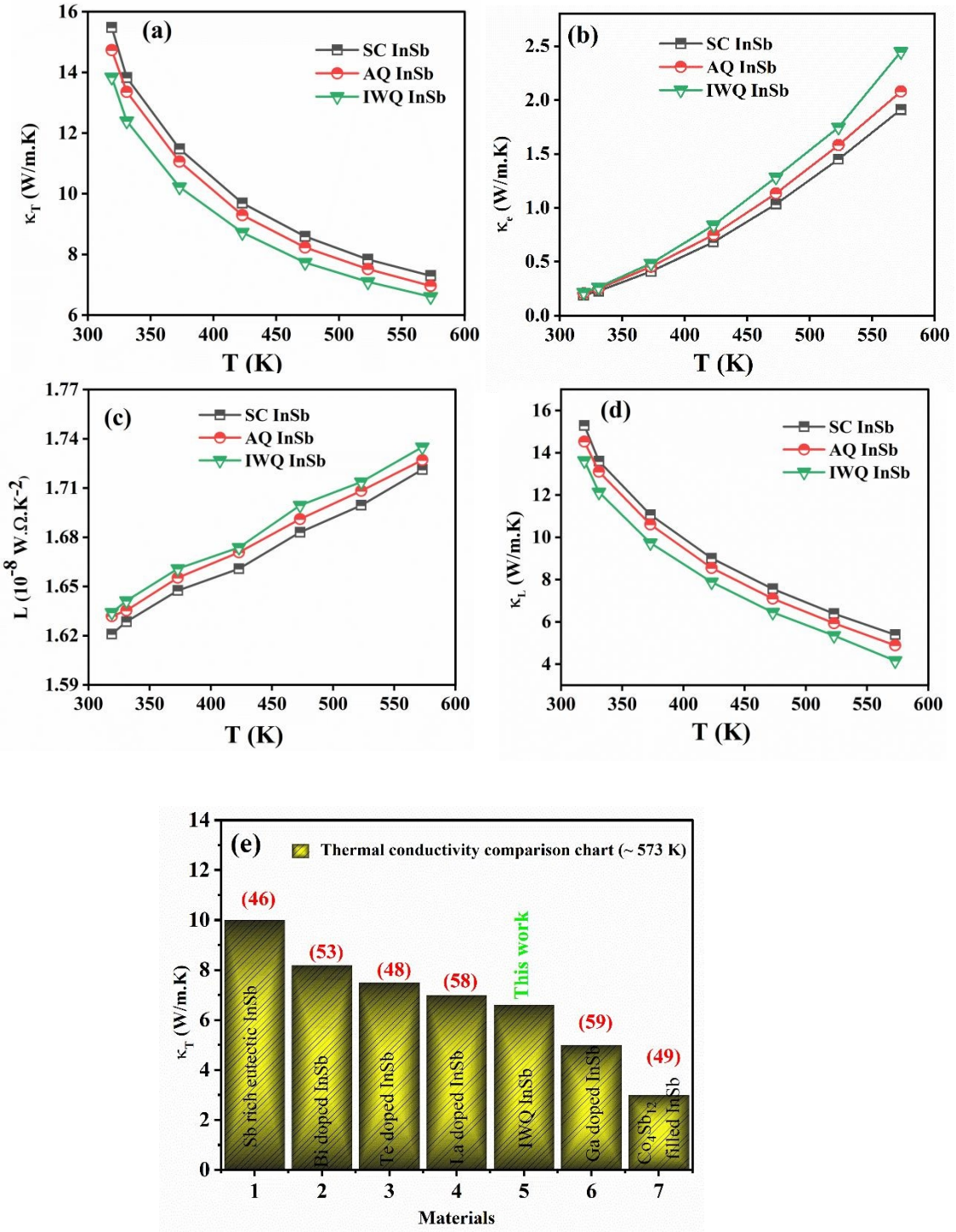

Fig. 8 (a-e): Total thermal conductivity (κ_T) (a), electronic thermal conductivity (κ_e) (b), lattice thermal conductivity (κ_L)(c), Temperature dependent Lorentz number (L) (d) of InSb samples with cooling rates as a function of temperature and Thermal conductivity comparison for various reported values (e).

Furthermore, as evident from XRD analysis, the increased structural disorder promotes phonon scattering, leading to reduced κ_L. The broadening of peaks and lower wavenumber shifts in the Raman spectra (Fig. 4) further confirm the lattice

View Article Online
DOI: 10.1039/D6MA00062B

distortion in the IWQ sample compared to the SC sample. As shown in EBSD images (Fig. 3 (a_1-c_2)), the IWQ InSb sample has smaller sized grains compared to the SC InSb sample. As a result, the IWQ InSb sample has a greater number of grain boundaries, as seen in Fig.3 (c_1,c_2), which are responsible for scattering of phonons very effectively, leading to decreased κ_L. The schematic diagram of the phonon scattering mechanism is shown in Fig. 9.

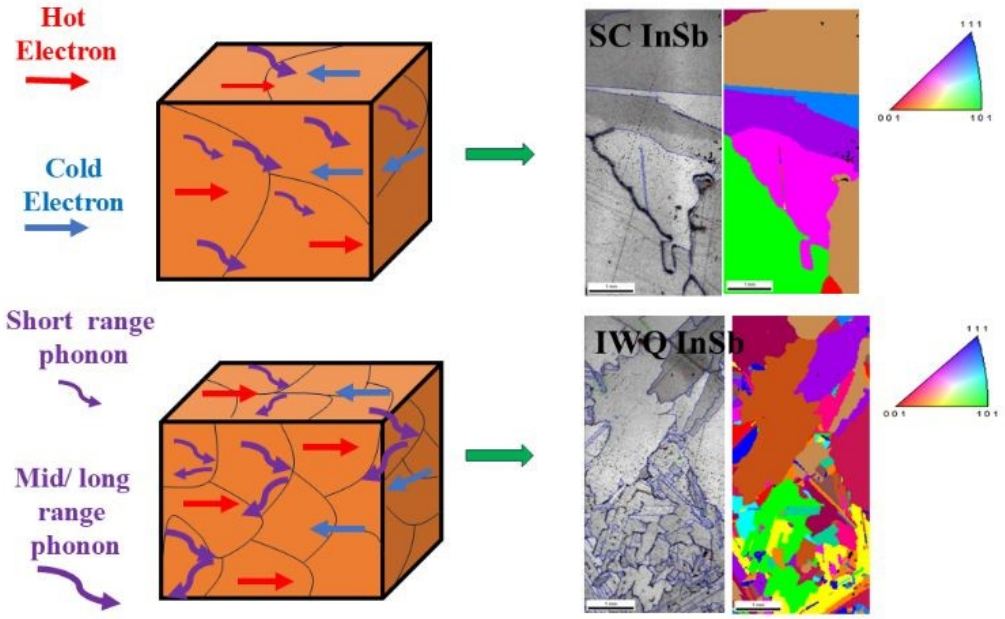

Fig. 9: Schematic representation of phonon scattering mechanisms SC InSb and IWQ InSb samples.

3.8 Figure of Merit of InSb ingots with different cooling rates:

Fig. 10 (a) demonstrates the zT of the prepared InSb samples with various cooling rates as a function of temperature. The zT was calculated using the PF and κ as a function of temperatures. To obtain a high zT, an extremely high PF and low κ_L are essential. Among all the samples, the IWQ InSb sample shows high PF and low κ. As a result, a higher zT of 0.60 was achieved at 573 K for the IWQ InSb sample compared to the SC InSb sample (zT of 0.46 at 573 K). The zT values were compared with the previous literature, as shown in Fig. 10 (b) [46,48,49,53,58,59]. The obtained zT values are relatively higher than that of reported similar materials.

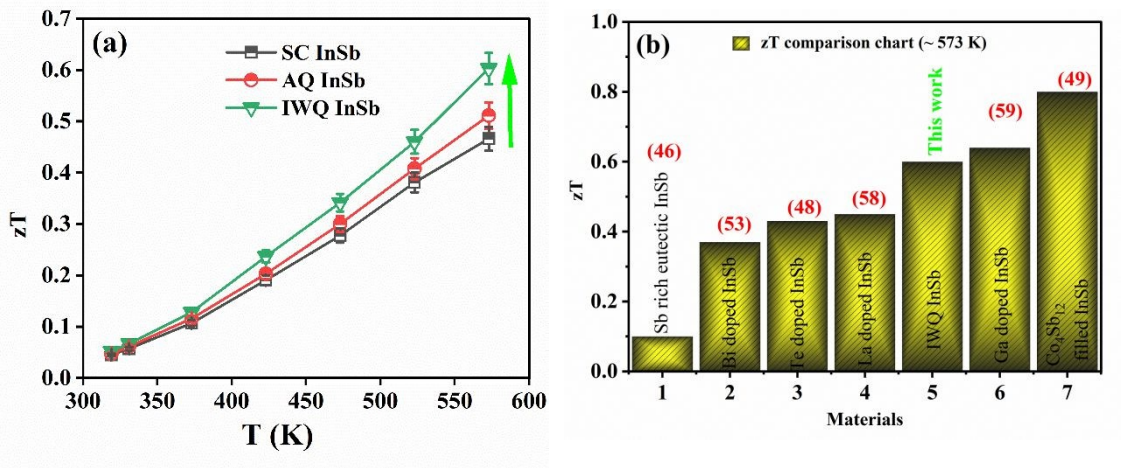

Fig. 10: zT value of InSb samples (a) with cooling rate as a function of temperature and comparison chart for various reported work (b).

View Article Online
DOI: 10.1039/D6MA00062B

4. Conclusion:

The polycrystalline InSb samples were prepared by the melt quenching technique under different cooling rates. The structural and surface morphological investigation of the samples has been extensively carried out by XRD, FESEM. The ρ slightly decreased with increasing cooling rates. The S of the prepared InSb samples was measured up to 573 K. A high-PF of 6951 μW/m K^2 was achieved for the IWQ InSb sample at 573 K compared to the SC InSb sample (5935 μW/m K^2 at 573 K). κ_T is reduced for the IWQ InSb sample (6.60 W/m/K) compared to SC InSb (7.29 W/m. K) at 573 K due to modification in the grain structures and grain boundary densities which enhanced the phonon scattering in the IWQ sample. As a result, a high zT of 0.60 was achieved at 573 K for the IWQ InSb sample compared to the SC InSb sample (zT of 0.46 at 573 K). The experimental results demonstrated that the grain structure modification through melt quenching process is an effective approach for enhancing the TE performance of InSb.

Author contributions

M. Sivakumar: conceptualization, methodology, formal analysis, investigation, validation, data curation, writing – original draft. **J. Prasath**: formal analysis, investigation. **S. Senthamizh Raja:** investigation**,** formal analysis. **R. Annie Victoria Rose**: formal analysis, investigation. J. **Mani**: formal analysis, investigation. **L.C. Chuang:** formal analysis, investigation, validation. **Sri Sai Samhitha Gadhavajhala**: formal analysis, data curation. **Bhuvanesh Srinivasan:** investigation, formal analysis, writing-review & editing**. R. Jayavel:** resources, writing – review & editing. **K. Fujiwara:** formal analysis, investigation, review & editing validation **M. Arivanandhan**: conceptualization, project administration, resources, writing – review & editing, supervision.

Conflicts of interest

There are no conflicts to declare.

Data availability

The data supporting the findings of this study are available within the article and its supplementary information (SI). Additional raw data available from the corresponding author upon reasonable request. Supplementary information is available for the separate attachment (SI).

Acknowledgements

This work was supported by the DST-INSPIRE Fellowship with inspire code IF200541 awarded to M.S. The author, M.S., would like to acknowledge the support from the Department of Science and Technology (DST), New Delhi, Government of India, for the award of DST Inspire Fellowship (Reference No: DST/INSPIRE FELLOWSHIP/2020/IF200541). The work is financially supported by the GIMRT collaborative project (202308-RDKGE-0536, 202408-RDKGE-0534), Tohoku University, Sendai, Japan. S.S.S.G. thanks PMRF for the fellowship. B. S. thanks the Anusandhan National Research Foundation (ANRF / erstwhile SERB) for the funding (File Numbers SRG/2023/002282 and CRD/2024/000912) and IIT-Madras for the seed grant (NFSG).

References:

1 Y. Li, X. Wang, D. Luo, Y. Shi, Y. Ren and Y. Yan, *e-Prime - Advances in Electrical Engineering, Electronics and Energy*, DOI:10.1016/j.prime.2023.100180.

2 T. Hong, C. Guo, D. Wang, B. Qin, C. Chang, X. Gao and L. D. Zhao, *Mater. Today Energy*, DOI:10.1016/j.mtener.2022.100985.

3 Z. G. Chen, G. Hana, L. Yanga, L. Cheng and J. Zou, *Elsevier B.V.*, 2012, preprint, DOI: 10.1016/j.pnsc.2012.11.011.

4 L. Wang, T. Chu, S. Yuan, P. Zou, W. Zhai, X. Zheng and M. Xia, *Elsevier Ltd*, 2025, preprint, DOI: 10.1016/j.enconman.2025.119621.

View Article Online
DOI: 10.1039/D6MA00062B

5 A. P. Sobha and S. K. Narayanankutty, *IEEE Trans. Nanotechnol.*, 2014, **13**, 835–841.

6 O. Caballero-Calero, J. R. Ares and M. Martín-González, *John Wiley and Sons Inc*, 2021, preprint, DOI: 10.1002/adsu.202100095.

7 H. Mamur, Ö. F. Dilmaç, J. Begum and M. R. A. Bhuiyan, *Elsevier Ltd*, 2021, preprint, DOI: 10.1016/j.clema.2021.100030.

8 R. Singh, S. Dogra, S. Dixit, N. I. Vatin, R. Bhardwaj, A. K. Sundramoorthy, H. C. S. Perera, S. P. Patole, R. K. Mishra and S. Arya, *Elsevier B.V.*, 2024, preprint, DOI: 10.1016/j.hybadv.2024.100176.

9 Y. Liu, G. Song, K. Tai, Z. Yu, Y. Ran, J. He and Y. Wu, *Thin Solid Films*, DOI:10.1016/j.tsf.2024.140585.

10 L. Huang, Y. Zheng, L. Xing and B. Hou, *Elsevier Ltd*, 2023, preprint, DOI: 10.1016/j.tsep.2023.102064.

11 S. H. Zaferani, M. W. Sams, R. Ghomashchi and Z. G. Chen, *Elsevier Ltd*, 2021, preprint, DOI: 10.1016/j.nanoen.2021.106572.

12 Z. Zhou, J. Yang, Q. Jiang, Y. Luo, D. Zhang, Y. Ren, X. He and J. Xin, *J. Mater. Chem. A Mater.*, 2016, **4**, 13171–13175.

13 A. Sampathu, M. Sivakumar, R. Chellakumar, D. Narendran, J. Kasthuri, S. Kumaran, M. Arivanandhan and M. Balakrishnan, *Mater. Sci. Semicond. Process.*, DOI:10.1016/j.mssp.2025.110284.

14 P.H.M. Böttger, K. Valset, S. Deledda, T.G. Finstad, J. Electron. Mater. 39 (2010) 1583–1588. https://doi.org/10.1007/s11664-010-1269-2.

15 Y. Yu, C. Zhou, T. Ghosh, C.F. Schön, Y. Zhou, S. Wahl, M. Raghuwanshi, P. Kerres, C. Bellin, A. Shukla, O. Cojocaru-Mirédin, M. Wuttig, Advanced Materials 35 (2023).

16 Y. Yu, C. Zhou, T. Ghosh, C. F. Schön, Y. Zhou, S. Wahl, M. Raghuwanshi, P. Kerres, C. Bellin, A. Shukla, O. Cojocaru-Mirédin and M. Wuttig, *Advanced Materials*, DOI:10.1002/adma.202300893.

17 Q. Xiong, G. Han, G. Wang, X. Lu and X. Zhou, *John Wiley and Sons Inc*, 2024, preprint, DOI: 10.1002/adfm.202411304.

18 Q. Jian, Y. Gong, C. Chen, R. Sun, S. Zhao, T. Shen, Q. Zhang, Y. Geng, Y. Li, W. Dou, C. Liang, Y. Liu, D. Xiang, P. Ying and G. Tang, *ACS Appl. Mater. Interfaces*, 2025, **17**, 15527–15534.

19 J. Chen, L. Wang, D. Ren, Y. Chu, Y. Wu, K. Meng, J. Miao, X. Xu and Y. Jiang, *Synth. Met.*, 2018, **239**, 13–21.

20 W. Li, Z. Yu, C. Liu, Y. Peng, B. Feng, J. Gao, G. Wu, X. Bai, J. Chen, X. Wang and L. Miao, *Journal of Advanced Ceramics*, 2023, **12**, 1511–1520.

21 L. L. Huang, J. Zhang, Z. M. Wang, X. G. Zhu, J. M. Li, C. Zhu, D. Li, C. J. Song, H. X. Xin and X. Y. Qin, *Materialia (Oxf).*, 2018, **3**, 169–173.

22 L. Xie, H. Tong, G. Peng, H. Wu, W. Shi, K. Yu, J. Hu, L. Jiao, X. Dong, F. Guo, W. Cai, Y. Zhang, H. Wu, Z. Liu and J. Sui, *Nature Communications* , DOI:10.1038/s41467-025-62902-8.

23 V. C. S. Theja, V. Karthikeyan, D. S. Assi, H. Huang, C. H. Shek and V. A. L. Roy, *Advanced Energy and Sustainability Research*, DOI:10.1002/aesr.202300125.

24 V.P. Kannan, V. Lourdhusamy, I. Paulraj, C.J. Liu, M. Sridharan, ACS Appl. Mater. Interfaces 15 (2023) 47058–47069. https://doi.org/10.1021/acsami.3c10418.

25 S. Perumal, S. Roychowdhury and K. Biswas, *Inorg. Chem. Front.*, 2016, **3**, 125–132.

26 Q. Wang, Z. Li, L. Xu, T. Jiang, J. Wang, X. Qian and S. Wang, *Materials Today Physics*, DOI:10.1016/j.mtphys.2022.100818.

27 Q. Zhang, Z. Xiong, J. Jiang, W. Li, G. Xu, S. Bai, P. Cui and L. Chen, *J. Mater. Chem.*, 2011, **21**, 12398–12401.

28 Y. Luo, J. Yang, Q. Jiang, W. Li, Y. Xiao, L. Fu, D. Zhang, Z. Zhou and Y. Cheng, *Nano Energy*, 2015, **18**, 37–46.

29 C. Wang, D. Cong, G. Tang, X. Zhou and J. Li, *Chemical Engineering Journal*, DOI:10.1016/j.cej.2024.154313.

30 Q. Q. Wang, K. F. Liu, Y. Y. Su, X. C. Liu, Q. Liu, S. Zhou, J. Liu and S. Q. Xia, *Acta Mater.*, DOI:10.1016/j.actamat.2023.119028.

31 K. Zhang, Y. Huang, S. Liu, Q. Xiong, S. Zheng, B. Zhang, G. Wang, Y. Pan, G. Han, G. Wang, X. Lu, X. Chen and X. Zhou, *Advanced Materials*, DOI:10.1002/adma.202503496.

32 N. Grevtsov, E. Chubenko, V. Bondarenko, I. Gavrilin, A. Dronov, S. Gavrilov, D. Goroshko, O. Goroshko, G. Rymski, K. Yanushkevich, Mater. Res. Bull. 184 (2025).

33 T. Zhu, K. Swaminathan-Gopalan, K. Stephani and E. Ertekin, *Phys. Rev. B*, DOI:10.1103/PhysRevB.97.174201.

34 T. Palasyuk, C. Jastrzebski, A. Khachapuridze, E. Litwin-Staszewska, T. Suski, I. Grzegory and S. Porowski, *Physica Status Solidi - Rapid Research Letters*, DOI:10.1002/PSSR.202400093.

35 R. Abinaya, J. Archana, S. Harish, M. Navaneethan, C. Muthamizhchelvan, S. Ponnusamy, H. Udono, R. Sugahara, Y. Hayakawa and M. Shimomura, *J. Colloid Interface Sci.*, 2021, **584**, 295–309.

36 D. K. Meena, R. S. C. Bose, S. Vinoth, K. Annapurna and K. Ramesh, *Appl. Phys. A Mater. Sci. Process.*, DOI:10.1007/s00339-022-05662-2.

37 X. Tang, Z. Li, W. Liu, Q. Zhang and C. Uher, *John Wiley and Sons Inc*, 2022, preprint, DOI: 10.1002/idm2.12009.

38 J. D. Henderson, L. Pearson, H. Y. Nie and M. C. Biesinger, *Surface and Interface Analysis*, 2025, **57**, 81–97.

39 A. Vishwakarma, N. S. Chauhan, R. Bhardwaj, K. K. Johari, S. R. Dhakate, B. Gahtori and S. Bathula, *J. Electron. Mater.*, 2021, **50**, 364–374.

40 S. Perumal, M. Samanta, T. Ghosh, U. S. Shenoy, A. K. Bohra, S. Bhattacharya, A. Singh, U. V. Waghmare and K. Biswas, *Joule*, 2019, **3**, 2565–2580.

41 C. Liu, Z. Zhang, Y. Peng, F. Li, L. Miao, E. Nishibori, R. Chetty, X. Bai, R. Si, J. Gao, X. Wang, Y. Zhu, N. Wang, H. Wei and T. Mori, *Charge transfer engineering to achieve extraordinary power generation in GeTe-based thermoelectric materials*, 2023.

42 V. Nirmal Kumar, Y. Hayakawa, H. Udono and Y. Inatomi, *Intermetallics (Barking).*, 2019, **105**, 21–28.

43 Y. Chen, X. L. Shi, D. Li, J. Zhu, M. Li, L. Zhang, Z. Zhang, Z. Feng, X. Ma, H. Zhong, S. Li and Z. G. Chen, *Acta Mater.*, DOI:10.1016/j.actamat.2025.120736.

44 M. Jin, X. Bai, Z. Tang, S. Zhao, Y. Chen, L. Zhou, Y. Peng, X. Chen and X. Xu, *Mater. Res. Bull.*, DOI:10.1016/j.materresbull.2021.111411.

45 D. Besson, M. Treilleux, A. Hoareau and C. Esnouf, *Philosophical Magazine A: Physics of Condensed Matter, Structure, Defects and Mechanical Properties*, 2000, **80**, 1139–1149.

46 Y. Cheng, J. Yang, Q. Jiang, D. He, J. He, Y. Luo, D. Zhang, Z. Zhou, Y. Ren and J. Xin, *J. Mater. Chem. A Mater.*, 2017, **5**, 5163–5170.

47 K. Wang, P. Qin, Z. H. Ge and J. Feng, *Mater. Lett.*, 2017, **209**, 373–375.

48 S. Yamaguchi, T. Matsumoto, J. Yamazaki, N. Kaiwa and A. Yamamoto, *Appl. Phys. Lett.*, 2005, **87**, 1–3.

49 S. Ghosh, S. M. Valiyaveettil, G. Shankar, T. Maity, K. H. Chen, K. Biswas, S. Suwas and R. C. Mallik, *ACS Appl. Energy Mater.*, 2020, **3**, 635–646.

50 W. Li, T. Xu, Z. Ma, Y. Cheng, J. Li, Q. Jiang, Y. Luo and J. Yang, *Mater. Today Energy*, DOI:10.1016/j.mtener.2022.101091.

51 M. Sivakumar, D. Sidharth, B. Srinivasan and M. Arivanandhan, *J. Alloys Compd.*, DOI:10.1016/j.jallcom.2024.176908.

52 L. L. Huang, J. Zhang, Z. M. Wang, X. G. Zhu, J. M. Li, C. Zhu, D. Li, C. J. Song, H. X. Xin and X. Y. Qin, *Materialia (Oxf).*, 2018, **3**, 169–173.

53 J. Palraj, M. Moorthy, S. Katlakunta and S. Perumal, *Ceram. Int.*, 2022, **48**, 29284–29290.

54 Z. Lu, B. Huang, G. Li, X. Zhang, Q. An, B. Duan, P. Zhai, Q. Zhang and W. A. Goddard, *NPJ Comput. Mater.*, DOI:10.1038/s41524-021-00581-x.

55 R. Annie Victoria Rose, D. Sidharth, M. Arivanandhan and R. Jayavel, *New Journal of Chemistry*, 2024, **48**, 11506–11517.

56 D. Sidharth, I. Paulraj, V. Lourdhusamy, M. Arivanandhan and C. J. Liu, *J. Eur. Ceram. Soc.*, 2024, **44**, 954–960.

57 D. Sidharth, B. Srinivasan, A. S. A. Nedunchezhian, P. Thirukumaran, M. Arivanandhan and R. Jayavel, *Journal of Physics and Chemistry of Solids*, DOI:10.1016/j.jpcs.2021.110303.

58 D. Zhang, H. Wu, Z. Zhou, S. Zheng, B. Zhang, Y. Zhou, X. Lu and X. Zhou, *Materials Today Physics*, DOI:10.1016/j.mtphys.2023.101020.

59 Z. Du, X. Chen, J. Zhu and J. Cui, *Current Applied Physics*, 2018, **18**, 893–897.

Data availability statement

View Article Online
DOI: 10.1039/D6MA00062B

The data supporting the findings of this study are available within the article and its supplementary information (SI). Additional raw data available from the corresponding author upon reasonable request.